
A probabilistic displacement hazard assessment framework for distributed ruptures from strike-slip earthquakes

Alba M. Rodriguez Padilla[1] and Michael E. Oskin[1]

[1] *Department of Earth and Planetary Sciences, University of California, Davis*

Abstract

Widespread distributed fracturing during earthquakes threatens infrastructure and lifelines. We combine high-resolution rupture maps from the five major surface-rupturing strike-slip earthquakes in southern California and northern Mexico since 1992 to incorporate the displacements produced by secondary ruptures into a probabilistic displacement hazard analysis framework. Through analysis of the spatial distribution of mapped ruptures and displacements for each of these events, we develop a magnitude-dependent expression for the probability per unit area of finding a secondary rupture that accommodates a displacement that exceeds a displacement threshold at a given distance away from the principal fault. Our model is best applied to estimating expected secondary displacements for strike-slip earthquakes, similar to those analyzed, with widespread ruptures across immature fault zones.

Key points

1. Strike-slip earthquakes on immature faults cause widespread ruptures that can threaten infrastructure.
2. We present a probabilistic fault displacement hazard model based on high-resolution surface rupture maps and displacement measurements.
3. Our model may be used to estimate secondary rupture displacements for strike-slip events on immature faults.

Introduction

Displacements from surface-rupturing earthquakes directly threaten infrastructure and lifelines in tectonically active regions. Probabilistic fault displacement hazard analysis (PFDHA) addresses this challenge by providing estimates of the likelihood and distribution of surface displacements during fault rupture (e.g. Youngs et al., 2003; Petersen et al., 2011; Moss and Ross, 2011; Nurminen et al., 2020; Wang and Goulet, 2021). Over the past few years, earth scientists and engineers have joined efforts in standardizing fault displacement hazard models from empirical measurements collected after earthquakes (Baize et al., 2016; Baize et al., 2020; Sarmiento et al., 2021). The data these efforts are based on has improved due to increased coverage of surface rupturing earthquakes (e.g. airborne lidar, Chen et al., 2015; Hudnut et al., 2020), better post-earthquake response coordination (e.g. Mattioli et al., 2020), and advances in the repeat frequency and resolution of geodetic methods (e.g. Milliner and Donnellan, 2019; Xu et al., 2020).

We present a fault displacement model focused on distributed ruptures for strike-slip faults using data from five major surface rupturing earthquakes in the Eastern California Shear Zone and Northern Mexico. These events left behind impressive footprints of broadly distributed ruptures in the desert that have been carefully mapped: the Landers (1992), Hector Mine (1999), El Mayor-Cucapah (2010), and Ridgecrest (2019 foreshock and mainshock) earthquakes (Sieh et al., 1993; Lazarte et al., 1994; Treiman et al., 2002; Hudnut et al., 2002; Fletcher et al., 2014; Teran et al., 2015; Milliner et al., 2015; Milliner et al., 2016; Ponti et al., 2020; DuRoss et al., 2020; Rodriguez Padilla et al., 2022a). The hazard posed by secondary ruptures remains poorly characterized, challenging the ability of engineers and other stakeholders to evaluate the associated risk. In this contribution, we use surface rupture maps and displacement measurements from these well-documented earthquakes to fill this information gap. To do so, we develop a relationship for the probability per unit area of finding a rupture at a distance away from the principal fault that will have a displacement greater than a threshold. This relationship may be used by end-users to quantify surface displacement hazard in a probabilistic framework that can inform the design and evaluation of lifelines and engineered structures located near or across active fault zones.

1 Surface rupture and displacement measurements

The Fault Displacement Hazard Initiative (FDHI) database, hosted and maintained by the Natural Hazards Risk & Resilience Research Center at the University of California, Los Angeles, includes 66 surface-rupturing earthquakes, with moment magnitudes ranging from 5.0 to 8.0, of all faulting styles (Sarmiento et al., 2021). The database incorporates surface rupture maps and displacement measurements for each of the events. The ruptures are classified as primary and distributed. The slip measurements document magnitude and location, and, sometimes, direction.

We select five strike-slip events from the FDHI rupture database, the 1992 M_w7.3 Landers, 1999 M_w 7.1 Hector Mine, 2010 M_w 7.2 El Mayor-Cucapah, and 2019 Ridgecrest earthquakes (separated into $\mathrm{M_w}$ 6.4 foreshock and $\mathrm{M_w}$ 7.1 mainshock; Figure 1) to incorporate into our model. We choose these events because they are well-mapped, and they occurred on relatively immature faults (< 25 km cumulative displacement) that share the same regional tectonic setting (Eastern California Shear Zone and northern Baja California transtensional rift).

The surface rupture maps in the FDHI database include some variability in completeness and mapping style. Overall, the near-field section of these earthquakes (<1 km from the principal rupture trace) is mapped at a similar resolution, while the far-field has some variability in spatial completeness and resolution. Specifically, the rupture map for the El Mayor-Cucapah earthquake includes ruptures mapped from radar data at its northern end into southern California and its southern end through the Colorado River Delta (Figure 1)(Fletcher et al., 2014). We remove these radar-based features, which are mapped more simply than the field and lidar-based ruptures, and thus induce a biased population of long ruptures that increase far-field rupture density unrealistically. Similarly, the foreshock and mainshock Ridgecrest maps contain some features that are doubly mapped, of which we remove the simplified traces (Ponti et al., 2020; DuRoss et al., 2020).

A displacement model for secondary ruptures from surface rupture and displacement maps

We define probabilistic fault displacement hazard as the probability per unit area of finding a rupture at a distance x away from the principal fault with slip greater than a threshold S_0. Computing this probability requires knowledge of the spatial distribution of ruptures and the displacements that these ruptures could accommodate. We address the former through analysis of the distribution of rupture density and the latter by examining the distribution of surface displacements measured for each of our selected events. The fault displacement hazard results from the joint probability,

$$\begin{aligned} P(S > S_0|x, M_w) = P(rupture|x) \\ P(S > S_0|x, rupture, M_w), \end{aligned} \tag{1}$$

where $P(S > S_0|x, M_\mathrm{w})$ is the probability per unit area of finding a rupture at a distance away from the fault, resulting from an event of a given magnitude, that will have a displacement greater than the threshold S_0. $P(rupture|x)$ is the probability of rupture per unit area occurring at that location. $P(S > S_0|x, rupture, M_\mathrm{w})$ is the displacement exceedance, a probability of finding a displacement that exceeds that threshold at a given distance from the fault, given the presence of a rupture, for a given earthquake magnitude. Note that in fitting the second term in equation 1, we assume that all of the measured surficial displacements in the FDHI database are associated with discrete fault ruptures and not produced by other mechanisms, such as ground failure.
To assess the probability of observing a rupture (first term in equation 1), we use the surface rupture maps in the FDHI database. The probability of observing a rupture at a given distance away from the fault can be obtained from the spatial distribution of fracture density (e.g. Rodriguez Padilla et al., 2022b), which is given by the inverse power-law:

$$\nu(x) = \nu_o \left(\frac{x + x_f}{x_f} \right)^{-\gamma} \tag{2}$$

Where ν_o is the rupture density at the origin in number of ruptures per unit $1m^2$ area, x_f is a normalizing constant and related to the uncertainty of the location of the fault trace in meters (Rodriguez Padilla et al., 2022b) The exponent γ is the slope of the decay of rupture density with distance in log-log space, or scaling exponent. $\nu(x)$ is the probability of a rupture occurrence per unit $1m^2$ area.
We use equation 2 to calculate the rupture density distribution (and thus the probability of finding a rupture per unit area) for the Landers, Hector Mine, and El Mayor-Cucapah earthquakes (Figure 2). To do this, we discretize individual ruptures into 1-meter spaced points so that mapping choices do not bias the rupture density estimates (Rodriguez Padilla et al., 2022b). The principal rupture trace for each event (i.e. the fault with respect to which fault-perpendicular distance is measured) is simplified from the ruptures mapped as primary in each of the rupture maps in the FDHI rupture database (figure A1 in the appendix), with the exception of the Ridgecrest mainshock where a second fault in the middle of the dry lake bed was added based on the mapping of Rodriguez Padilla et al. (2022b). We fit each parameter in equation 2 to the rupture data using an ensemble sampler Monte Carlo Markov Chain (see supplementary methods section). The maximum likelihood fits and posterior distributions for x_{fr} and γ are shown in figure 2 and provided in table 1. Note that the rupture distributions are independent of earthquake magnitude, with all events having similar rupture densities ν_o at the fault, hence the magnitude-independence of the first term in equation 1.

To assess displacement exceedance (second term in equation 1), we include only the displacements in the FDHI database (supplementary figure A2) measured in the field, and exclude measurements derived from other techniques, such as image correlation. This is to ensure that the displacement measurements we consider are collected over apertures consistent with the width of individual ruptures. The vast majority of the displacements in the database are lateral and therefore record shear, with a minor portion of them recorded in absolute terms, where both lateral and vertical displacements are recorded as a ratio, representing a mixed-mode fracture. Because of the limited information available on fracture mode and displacement direction, our models are constructed without consideration of these parameters.

Coseismic displacements are highest along the principal fault trace and decline to lower values on distributed ruptures. We find that the mean values of displacement measurements from the FDHI database, binned with respect to distance to the principal fault trace, may be modeled as an inverse power-law described by:

$$\lambda(x) = \beta \left(\frac{x + x_S}{x_S} \right)^{-n} \tag{3}$$

where λ is the mean of the displacement at every distance bin, β is the average displacement at the origin, x is the location away from the principal fault trace, x_S is a normalization factor held constant at 1 meter (see supplementary methods in the appendix), and n is the slope of the relationship between mean displacement and distance in log-log space, or the scaling exponent. We fit equation 3 to the distribution of average displacements with distance for each of the events using an ensemble sampler for Monte-Carlo Markov Chain (see appendix for detailed method). The maximum likelihood fits and posterior distributions for β and n are shown in figure 3 and provided in table 1. Values of β range from 1.2 meters for the Ridgecrest foreshock to 4.4 meters for the Hector Mine event, broadly consistent with the average slip at the fault in each earthquake.

We find that the values of n agree between the different events, averaging around 0.45, though the fits vary in quality between events, with the Ridgecrest foreshock and the Hector Mine events being the least well characterized by equation 3. This poor characterization arises from the broader zone of similar average displacement measurements near the principal fault trace, and much higher scatter in the further ($<$ 1 km from the fault in Hector Mine and $<$ 100 m from the fault in the Ridgecrest foreshock) displacements measured in the field (Figure 3). This is clear in the residuals of the fit of 3 to the field displacement data from these two events (figure A5 in the appendix). In the case of the Ridgecrest foreshock, the constant average displacement values near the intercept may arise from incomplete rupture to the surface, which may be a magnitude-dependent characteristic. This is something we do not consider in our model.

The scaling exponent, n, that describes the spatial distribution of mean displacement is very consistent for the Ridgecrest mainshock, the Landers, and the El Mayor-Cucapah events, and these events exhibit low residuals for the fit of equation 3 to the field displacement data (figure A5 in the appendix).

Within each distance bin, we find that the population of field displacement measurements is well described by an exponential distribution (Figure 4). This relationship holds up remarkably well for all of the distance bins analyzed, as shown by the observation of similar values for the mean and the standard deviation of displacement measurements within each bin (supplementary figure A3). The distribution of displacements within a distance bin can thus be described as follows:

$$f(S|x) = \frac{1}{\lambda} e^{\frac{-S}{\lambda}} \tag{4}$$

where λ, the mean of the displacement at every distance bin, is the output of equation 3. Combining equations 3 and 4 yields:

$$f(S) = \frac{1}{\beta}\left(\frac{x+x_S}{x_S}\right)^n e^{-\frac{S}{\beta}\left(\frac{x+x_S}{x_S}\right)^n} \tag{5}$$

Equation 5 is a probability density function (PDF) of observed displacements with distance from the principal fault trace. We integrate this PDF from S_0, the threshold displacement of interest, to S_{max}, the maximum observed slip in an event (note that we expect $S_{max} \geq \beta$), to solve for the probability of observing a displacement that exceeds S_0 on an observed rupture given an earthquake magnitude (second term of equation 1):

$$\begin{aligned} P(S > S_0|x, rupture, M_w) &= \int_{S_0}^{S_{max}} \frac{1}{\beta}\left(\frac{x+x_S}{x_S}\right)^n \\ &\qquad e^{-\frac{S}{\beta}(\frac{x+x_S}{x_S})^n} dS \\ &= -e^{-\frac{S}{\beta}(\frac{x+x_S}{x_S})^n}\Big|_{S_0}^{S_{max}} \end{aligned} \tag{6}$$

Note that in evaluating this integral, the term containing S_{max} is small, so that as long as $S_0 << S_{max}$, this term can be ignored. This limits the appropriate application of our model to predicting the probability of secondary displacements above a threshold that is a fraction (i.e. 10%) of the slip measured on the primary fault trace. This limitation is appropriate because solving only for the probability of large slip values would be akin to predicting the presence of another primary fault trace, which is not the objective of this model. With this application in mind, completing the integration of equation 6 yields:

$$P(S > S_0|x, rupture, M_w) = e^{\frac{-S_0}{\beta}(\frac{x+x_S}{x_S})^n} \tag{7}$$

The displacement threshold, S_0, may be adjusted by end-users for different engineering applications. Combining the probabilities in equations 2 and 7 yields the solution to equation 1:

$$P(S > S_0|x, M_w) = \nu_o\left(\frac{x+x_f}{x_f}\right)^{-\gamma} e^{\frac{-S_0}{\beta}\left(\frac{x+x_S}{x_S}\right)^n} \tag{8}$$

Note that the magnitude-dependence in this model arises from parameter β, the average displacement on the fault.

Figure 5 shows the relationship in equation 8 for each dataset for x= 1 to x=10 kilometers away from the fault, consistent with the extent of ruptures shown in Figure 2, with example values of S_0 of 0.01, 0.1, and 0.5 meters. The probabilities of finding a rupture that hosts displacements larger than 1 mm near the fault exceed 10% for all of the events considered here, reaching 20% for the Ridgecrest foreshock (Figure 5, left). Despite the smaller magnitude, the Ridgecrest foreshock has the highest rupture density at the fault, which results in higher probabilities $P(S > S_0)$, despite the lower value of β, at this displacement threshold. $P(S > S_0)$ decreases rapidly with distance for all events, even for this small value of S_0, such that the probability of finding a rupture that hosts a displacement larger than 1 mm is lower than 1 in 1,000 beyond 10 km from the primary fault trace.

The surface rupture hazard curves for the Ridgecrest mainshock, Landers, El Mayor-Cucapah, and Hector Mine events look very similar for $S_0 = 1$ cm to those for $S_0 = 1$ mm. The variability of $P(S > S_0)$, about a factor of 2, at the intercept, arises largely from the variability in rupture density for the different events and likely reflects the natural variability that may be expected for these events and low displacement thresholds, regardless of magnitude (Figure 5, center). The magnitude-dependence of the model becomes clear with increasing distance away from the fault, given by the larger slope of $P(S > S_0)$ for the smaller-magnitude Ridgecrest foreshock. This pattern becomes even more obvious for the $P(S > S_0)$ curves where $S_0 = 0.5$ meters (Figure 5, right). At this displacement threshold, the effect of magnitude, captured by parameter β, trumps that of rupture density at the intercept and the Ridgecrest foreshock has a lower probability of finding a rupture hosting a displacement larger than 0.5 meters than that of the mainshock or Landers. When $S_0 = 0.5$ m, $P(S > S_0)$ becomes lower than 1 in 10,000 at about 1 km away from the fault for the Ridgecrest mainshock, the Landers, the Hector Mine, and the El Mayor-Cucapah events. This hazard level is crossed at about 200 m from the fault for the Ridgecrest foreshock.

A generalized rupture-displacement probability model

The individual models of $P(S > S_0)$ for each event (figure 5) can be used to inform a general model that is representative of events like these, i.e., those dominated by distributed deformation, largely rupturing through sediment, hosted on immature fault zones.

To estimate the first term of $P(S > S_0)$ for the general model, which is independent of earthquake magnitude, we combine the rupture distributions from the FDHI database from these five earthquakes and estimate a general relationship for rupture density with fault-perpendicular distance using equation 2 (figure A4 in the appendix). This is possible because the parameters describing the spatial distributions of rupture density for all events overlap within error, irrespective of magnitude or other event characteristics.

The second term in $P(S > S_0)$ is magnitude-dependent and therefore requires more careful examination to be generalized. The scaling exponent, n, that describes the spatial distribution of mean displacement is very consistent for the M_w 7.1 Ridgecrest mainshock, the M_w 7.3 Landers, and the M_w 7.2 El Mayor-Cucapah events, and the distribution of field displacements for these events is well described by equation 3, as captured by the low residuals (figure A5 in the appendix). Thus, to estimate n in our general model, we combine the posterior distributions of n from the Landers, El Mayor-Cucapah, and Ridgecrest mainshock displacement distributions (figure A6 in the appendix). We find that n is normally distributed with a mean value of 0.44 and a standard deviation of 0.08.

The magnitude-dependence of our probabilistic displacement model arises from parameter β, which we propose may be estimated using the empirical relationship for average displacement as a function of magnitude from Brengman et al. (2019):

$$\beta = 10^{\frac{M_w - a}{b}} \tag{9}$$

where a =6.5197 $\pm$ 0.131 and b = 1.0824 $\pm$ 0.2323 are the regression coefficients determined by Brengman et al. (2019) for strike-slip earthquakes.

Two examples of the general model are shown in Figure 6. One for events of $M_w = 6$, 6.5, 7 and 7.5, all with $S_0 = 0.1$ m (Figure 6, left), and a second for values of $S_0 = 0.01$, 0.1, 0.5, and 1 m for an M_w 7 event (Figure 6, right). The magnitude dependence of $P(S > S_0)$ for a fixed displacement threshold S_0 manifests as an increasingly wider hazard envelope, i.e. slope and intercept increase proportionally with magnitude. For a fixed magnitude, the slope describing the probability $P(S > S_0)$ decreases with increasing displacement threshold S_0, and the intercept increases with decreasing values of S_0.

Parameter error estimates

The parameters that build our probabilistic displacement model $P(S > S_0)$ have uncertainties that must be accounted for. The sources of uncertainty in the model are the fitting error in the exponent n that describes the PDF of displacements for an event, the uncertainty in the average displacement at the fault, β, which combines the errors in parameters a and b from equation 9 (Brengman et al., 2019), and the uncertainty in the fits to x_{fr}, v_o, and γ which describe the spatial distribution of rupture density.

To combine the errors in both terms in equation 8, we make a prediction for $P(S > S_0)$ under each set of samples from our suite of 5000 combined parameter sets. The parameters in the first term of equation 8, which describe the spatial distribution of rupture density, are correlated, so they must be sampled from the same state of the Markov chain for this correlation to be preserved. The parameters in the displacement term in equation 8 are normally distributed. To consider the variability of n and β (a and b) in our uncertainty estimates, we draw random samples from a normal distribution where the best fit of each parameter is the mean and the standard deviation is the standard error of n for a and b reported in Brengman et al. (2019), and the standard deviation of n as calculated here (figure A6 in the appendix).

A general model with $S_0 = 0.1$ m and M_w 7, with uncertainties, as well as the model residuals resulting from the 5000 iterations of Monte Carlo sampling are shown in figure 7. The uncertainty distributions of each parameter are shown in figure A7 in the appendix. The incompleteness of the rupture maps in the far field contributes to the conical shape of the uncertainty distribution, which is largely inherited from the uncertainty in the rupture density and average displacement scaling exponents, γ and n. We estimate the one standard error by estimating the envelope of model fits at the 16^{th} and 84^{th} percentiles (1σ). Based on these envelopes, we expect variability in probability below one order of magnitude for $P(S > S_0)$ within 3 kilometers of the fault, increasing to 1.5 orders of magnitude at 10 km away from the fault. The standard error can be described by the expression:

$$\sigma_M = \tau e^{x^{0.15}} \tag{10}$$

where $\tau \approx 3x10^{-2}$ for the 84% percentile and $\tau \approx -4x10^{-2}$ for the 16% percentile. The fits of equation 10 to the model fits are shown in Figure 7 (bottom).

We provide a Jupyter Notebook (see data and resources) that allows end-users to generate their own model for $P(S > S_0)$. The only inputs required are a displacement threshold S_0 and an earthquake moment magnitude (M_w). The model outputs $P(S > S_0)$ curves with a best-fit model and an analytically defined uncertainty range using 10.

Model discussion and limitations

The model we develop in this contribution uses input rupture maps and field displacement measurements from select events in the Eastern California Shear Zone and northern Baja California. From our limited number of available surface rupturing events with high-resolution maps, there arises some challenges and assumptions in this model that limit its application. The events we cover here span the M_w 6.4-7.3 range. Within this range, we find that, surprisingly, the distribution of rupture density is not magnitude-dependent. However, this could change with an expanded dataset of high-resolution maps from more events. We find that with the data available that the secondary rupture densities at the principal fault vary by less than a factor of 10. The rupture density variability documented by Rodriguez Padilla et al. (2022b) between different portions of the Ridgecrest 2019 surface ruptures, which they found to be independent of the displacement magnitude at the surface, exceeds this level of variability. Hence there is no basis at this time to develop a magnitude-dependent estimator of secondary rupture density.

The magnitude-dependence in the models for individual events and for our general model arises from parameter β, the expected average displacement measured at the primary fault. This parameter separates the Ridgecrest foreshock from the other events distinctly. For the other, M_w 7.1 to 7.3 events, the variability in predicted average displacement at the fault is essentially indistinguishable.

Proper identification of the principal rupture trace is fundamental for the appropriate application of our model. The assumption of $S_0 << S_{max}$ in this model, required to obtain the expression in equation 7, underscores that our model is not appropriate to deduce the probability of large slip on a secondary rupture. This is a minor limitation in the sense that, a second rupture hosting a large slip is likely to be identified as an additional principal fault trace. Examples of this kind of categorization exist for the Ridgecrest mainshock and the El Mayor-Cucapah events (see figure A1 in the appendix), where multiple, parallel ruptures are classified as principal fault traces.

Even when the principal rupture trace has been properly localized, there remains a small knee in the curve of $P(S > S_0)$ in the very near-fault region, inherited from parameter x_{fr} in the expression that describes the distribution of rupture density (equation 2). x_{fr} captures the uncertainty in the location of this primary rupture trace and is on the order of a few meters for the events with high-resolution maps we use in this study. The uncertainty in the fault location is an important parameter to consider in PFDHA frameworks (e.g. Chen and Petersen, 2019). We expect that the uncertainty in the principal fault trace location for faults without recent surface ruptures should be, at a minimum, comparable to the values of x_{fr} deduced from these datasets. Thus, we consider x_{fr} a useful parameter to incorporate into our model, as it results in a more conservative, wider zone of, high $P(S > S_0)$ near the fault.

The Landers, Hector Mine, Ridgecrest, and El Mayor-Cucapah earthquakes show similar rupture distributions. The slopes (γ) or scaling exponents of rupture density that yield the probability of finding a rupture at a given distance away from the fault overlap within error (Figure 2), though the exponents for the Ridgecrest foreshock and mainshock are comparatively lower than those for the other events. We suspect the gentler slope of the Ridgecrest events partly results from the inclusion of far-field features mapped as simplified lines based on geodetic observations, and from the more thorough far-field coverage during the field mapping. The variation of rupture densities at distances beyond 3 kilometers away from the main rupture likely results from variable mapping extent (e.g. far-field coverage is not complete for each event), where the more complete far-field mapping during the Ridgecrest events contributes to the more gentle scaling exponent in those distributions. Incomplete far field map coverage is accounted for in our uncertainties and reflected in the increase in uncertainty in our model with fault-perpendicular distance seen in Figure 7 (bottom).

An important consideration regarding our model uncertainties is that the posterior distributions shown in Figures 3 and 2 only represent how well the models (equations 2 and 3) fit the spatial distributions of rupture density and average displacement. These distributions omit the epistemic uncertainty carried by these rupture maps and displacement measurements, which is associated with variability in mapping completeness throughout, as well as in individual mapper decisions when deciding where to place ruptures. The displacement distributions are also affected by the individual location errors for each displacement measurement. We expect larger location errors in the displacement measurements from the Landers and Hector Mine events, which predate the relaxation of selective availability for GPS locations.

The epistemic uncertainties in these models could be largely mitigated through the data collection process in future surface-rupturing earthquakes. In the case of the rupture distributions, even coverage of the area surrounding the fault should largely reduce the far-field variability in the distributions. For the displacements, more careful documentation of the complete displacement range within the fault zone, without bias toward larger displacements, is necessary. This could be achieved through even sampling of displacement measurements along the principal rupture zones. In addition, careful documentation of the direction of displacement and separation of horizontal and vertical components would enable an expansion of this model to include displacement direction, an important component of assessing rupture hazard to engineered structures.

The characteristics of the events considered in this study make our model suitable for application to other faults in immature fault zones (< 25 km of cumulative displacement) where large amounts of distributed deformation are expected, in landscapes dominated by extensive sediment cover. Our framework may not be appropriate for more mature fault zones with a higher degree of strain localization (Dolan and Haravitch, 2014). Because the bulk of the surface ruptures we analyze occurred in sediment, the application of this model for events predominantly in bedrock remains to be tested. Last, events with substantial blind faulting cause largely different distributed deformation patterns at the surface (e.g. Koehler et al., 2020), and therefore may not be well described by the model proposed here, which requires a principal fault trace to be distinguishable.

Conclusions

Using detailed rupture maps from the Ridgecrest, Landers, Hector Mine, and El Mayor-Cucapah earthquakes in southern California and northern Mexico, we develop a framework for PFDHA that estimates the probability of finding a rupture with a displacement exceeding a threshold S_0, located at a given distance away from a principal fault trace. This model may be best applied to assess rupture hazard for infrastructure in the near-field region (<3 km) of immature faults (<25 km of cumulative displacement) where widespread secondary fault ruptures are expected, such as in the Eastern California Shear Zone or the Walker Lake Belt of the western United States.

Acknowledgments

We thank Valère Lambert, Emily Brodsky, Kélian Dascher-Cousineau, and Magali Billen for discussions that improved this work. We are grateful to Chris Madugo for suggestions that enhanced the applicability of this model and to Alex Sarmiento for her help in navigating the FDHI database. This research was made possible largely with support from a PG&E research award. Rodriguez Padilla acknowledges support from NASA FINESST award 80NSSC21K1634. This is SCEC Contribution No. 11869.

Data and resources

The rupture maps are available from the FDHI rupture database appendix `https://www.risksciences.ucla.edu/girs-reports/2021/08)` (last accessed May 2022). The scripts used to generate the analysis in this paper and the Jupyter Notebook for end-users to work with our PFDHA framework are available from `https://github.com/absrp/strike_slip_PFDHA_model`.

References

1. Antoine, S. L., Klinger, Y., Delorme, A., Wang, K., Bürgmann, R., & Gold, R. D. (2021). Diffuse deformation and surface faulting distribution from submetric image correlation along

the 2019 Ridgecrest, California, ruptures. Bull. Seismol. Soc. Am., (5), 2275-2302.

2. Baize, S., Azuma, T., Champenois, J., Cinti, F., Civico, R., Costa, C., ... & Schwartz, D. (2017, November). Towards a unified and worldwide database of surface ruptures (SURE) for Fault Displacement Hazard Analyses. In Proceedings of the 8th International INQUA Meeting on Paleoseismology, Active Tectonics and Archeoseismology (PATA), Blenheim, New Zealand (pp. 13-16).

3. Baize, S., Nurminen, F., Sarmiento, A., Dawson, T., Takao, M., Scotti, O., ... & Villamor, P. (2020). A worldwide and unified database of surface ruptures (SURE) for fault displacement hazard analyses. Seismological Research Letters, 91(1), 499-520.

4. Brengman, C. M., Barnhart, W. D., Mankin, E. H., & Miller, C. N. (2019). Earthquake-scaling relationships from geodetically derived slip distributions. Bulletin of the Seismological Society of America, 109(5), 1701-1715.

5. Chen, T., Akciz, S. O., Hudnut, K. W., Zhang, D. Z., & Stock, J. M. (2015). Fault-Slip Distribution of the 1999 M w 7.1 Hector Mine Earthquake, California, Estimated from Postearthquake Airborne LiDAR Data. Bulletin of the Seismological Society of America, 105(2A), 776-790.

6. Chen, R., & Petersen, M. D. (2019). Improved implementation of rupture location uncertainty in fault displacement hazard assessment. Bulletin of the Seismological Society of America, 109(5), 2132-2137.

7. Dolan, J. F., & Haravitch, B. D. (2014). How well do surface slip measurements track slip at depth in large strike-slip earthquakes? The importance of fault structural maturity in controlling on-fault slip versus off-fault surface deformation. Earth and Planetary Science Letters, 388, 38-47.

8. DuRoss, C. B., Gold, R. D., Dawson, T. E., Scharer, K. M., Kendrick, K. J., Akciz, S. O., ... & Zinke, R. (2020). Surface displacement distributions for the July 2019 Ridgecrest, California, earthquake ruptures. Bulletin of the Seismological Society of America, 110(4), 1400-1418.

9. Fletcher, J. M., Teran, O. J., Rockwell, T. K., Oskin, M. E., Hudnut, K. W., Mueller, K. J., ... & González-García, J. (2014). Assembly of a large earthquake from a complex fault system: Surface rupture kinematics of the 4 April 2010 El Mayor–Cucapah (Mexico) Mw 7.2 earthquake. Geosphere, 10(4), 797-827.

10. Hart, E. 1994. Calico Fault and Adjacent 1992 Surface Ruptures near Newberry Springs, San Bernardino County. California Division of Mines and Geology Fault Evaluation Report, 238, California Geological Survey CD 2002-02.

11. Hudnut, K. W., Borsa, A., Glennie, C., & Minster, J. B. (2002). High-resolution topography along surface rupture of the 16 October 1999 Hector Mine, California, earthquake (M w 7.1) from airborne laser swath mapping. Bulletin of the Seismological Society of America, 92(4), 1570-1576.

12. Hudnut, K. W., Brooks, B. A., Scharer, K., Hernandez, J. L., Dawson, T. E., Oskin, M. E., ... & Sorhus, S. (2020). Airborne lidar and electro-optical imagery along surface ruptures of the 2019 Ridgecrest earthquake sequence, southern California. Seismological Research Letters, 91(4), 2096-2107.

13. Koehler, R. D., Dee, S., Elliott, A., Hatem, A., Pickering, A., Pierce, I., & Seitz, G. (2021). Field response and surface-rupture characteristics of the 2020 M 6.5 Monte Cristo range earthquake, Central Walker Lane, Nevada. Seismological Research Letters, 92(2A), 823-839.

14. Lazarte, C. A., Bray, J. D., Johnson, A. M., & Lemmer, R. E. (1994). Surface breakage of the 1992 Landers earthquake and its effects on structures. Bulletin of the Seismological Society of America, 84(3), 547-561.

15. Mattioli, G. S., Phillips, D. A., Hodgkinson, K. M., Walls, C., Mencin, D. J., Bartel, B. A., ... & Zaino, A. (2020). The GAGE data and field response to the 2019 Ridgecrest earthquake sequence. Seismological Research Letters, 91(4), 2075-2086.

16. Milliner, C. W., Dolan, J. F., Hollingsworth, J., Leprince, S., Ayoub, F., & Sammis, C. G. (2015). Quantifying near-field and off-fault deformation patterns of the 1992 Mw 7.3 Landers earthquake. Geochemistry, Geophysics, Geosystems, 16(5), 1577-1598.

17. Milliner, C. W. D., Dolan, J. F., Hollingsworth, J., Leprince, S., & Ayoub, F. (2016). Comparison of coseismic near-field and off-fault surface deformation patterns of the 1992 Mw 7.3 Landers and 1999 Mw 7.1 Hector Mine earthquakes: Implications for controls on the distribution of surface strain. Geophysical Research Letters, 43(19), 10-115.

18. Milliner, C., & Donnellan, A. (2020). Using daily observations from Planet Labs satellite imagery to separate the surface deformation between the 4 July Mw 6.4 foreshock and 5 July Mw 7.1 mainshock during the 2019 Ridgecrest earthquake sequence. Seismological Research Letters, 91(4), 1986-1997.

19. Milliner, C., Donnellan, A., Aati, S., Avouac, J. P., Zinke, R., Dolan, J. F., ... & Bürgmann, R. (2021). Bookshelf kinematics and the effect of dilatation on fault zone inelastic deformation: Examples from optical image correlation measurements of the 2019 Ridgecrest earthquake sequence. Journal of Geophysical Research: Solid Earth, 126(3), e2020JB020551.

20. Moss, R. E. S., & Ross, Z. E. (2011). Probabilistic fault displacement hazard analysis for reverse faults. Bulletin of the Seismological Society of America, 101(4), 1542-1553.

21. Nurminen, F., Boncio, P., Visini, F., Pace, B., Valentini, A., Baize, S., & Scotti, O. (2020). Probability of occurrence and displacement regression of distributed surface rupturing for reverse earthquakes. Frontiers in Earth Science, 8, 581605.

22. Petersen, M. D., Dawson, T. E., Chen, R., Cao, T., Wills, C. J., Schwartz, D. P., & Frankel, A. D. (2011). Fault displacement hazard for strike-slip faults. Bulletin of the Seismological Society of America, 101(2), 805-825.

23. Ponti, D. J., Blair, J. L., Rosa, C. M., Thomas, K., Pickering, A. J., Akciz, S., ... & Zinke, R. (2020). Documentation of surface fault rupture and ground-deformation features produced by the 4 and 5 July 2019 Mw 6.4 and Mw 7.1 Ridgecrest earthquake sequence. Seismological Research Letters, 91(5), 2942-2959.

24. Powers, P. M., & Jordan, T. H. (2010). Distribution of seismicity across strike-slip faults in California. Journal of Geophysical Research: Solid Earth, 115(B5).

25. Rodriguez Padilla, A. M., Quintana, M. A., Prado, R. M., Aguilar, B. J., Shea, T. A., Oskin, M. E., & Garcia, L. (2022a). Near-Field High-Resolution Maps of the Ridgecrest Earthquakes from Aerial Imagery. Seismological Society of America, 93(1), 494-499.

26. Rodriguez Padilla, A. M., Oskin, M. E., Milliner, C. W., & Plesch, A. (2022b). Accrual of widespread rock damage from the 2019 Ridgecrest earthquakes. Nature Geoscience, 15(3), 222-226.

27. Sarmiento, A., Madugo, D., Bozorgnia, Y., Shen, A., Mazzoni, S., Lavrentiadis, G., Dawson, T., Madugo, C., Kottke, A., Thompson, S., Baize, S., Milliner, C., Nurminen, F., Boncio, P., and Visini, F. (2021). Fault Displacement Hazard Initiative Database, UCLA B. John Garrick Institute for the Risk Sciences, Report GIRS-2021-08, doi: 10.34948/N36P48.

28. Sieh, K., Jones, L., Hauksson, E., Hudnut, K., Eberhart-Phillips, D., Heaton, T., ... & Zachariasen, J. (1993). Near-field investigations of the Landers earthquake sequence, April to July 1992. Science, 260(5105), 171-176.

29. Teran, O. J., Fletcher, J. M., Oskin, M. E., Rockwell, T. K., Hudnut, K. W., Spelz, R. M., ... & Morelan, A. E. (2015). Geologic and structural controls on rupture zone fabric: A field-based study of the 2010 Mw 7.2 El Mayor–Cucapah earthquake surface rupture. Geosphere, 11(3), 899-920.

30. Treiman, J. A., Kendrick, K. J., Bryant, W. A., Rockwell, T. K., & McGill, S. F. (2002). Primary surface rupture associated with the M w 7.1 16 October 1999 Hector mine earthquake, San Bernardino County, California. Bulletin of the Seismological Society of America, 92(4), 1171-1191.

31. Wang, Y., & Goulet, C. (2021). Validation of fault displacements from dynamic rupture simulations against the observations from the 1992 landers earthquake. Bulletin of the Seismological Society of America, 111(5), 2574-2594.

32. Wells, D. L., & Coppersmith, K. J. (1994). New empirical relationships among magnitude, rupture length, rupture width, rupture area, and surface displacement. Bulletin of the seismological Society of America, 84(4), 974-1002.

33. Xu, X., Sandwell, D. T., & Smith-Konter, B. (2020). Coseismic displacements and surface ruptures from Sentinel-1 InSAR: 2019 Ridgecrest earthquakes. Seismological Research Letters, 91(4), 1979-1985.

34. Youngs, R. R., Arabasz, W. J., Anderson, R. E., Ramelli, A. R., Ake, J. P., Slemmons, D. B., ... & Toro, G. R. (2003). A methodology for probabilistic fault displacement hazard analysis (PFDHA). Earthquake spectra, 19(1), 191-219.

469 ## 2 Figures

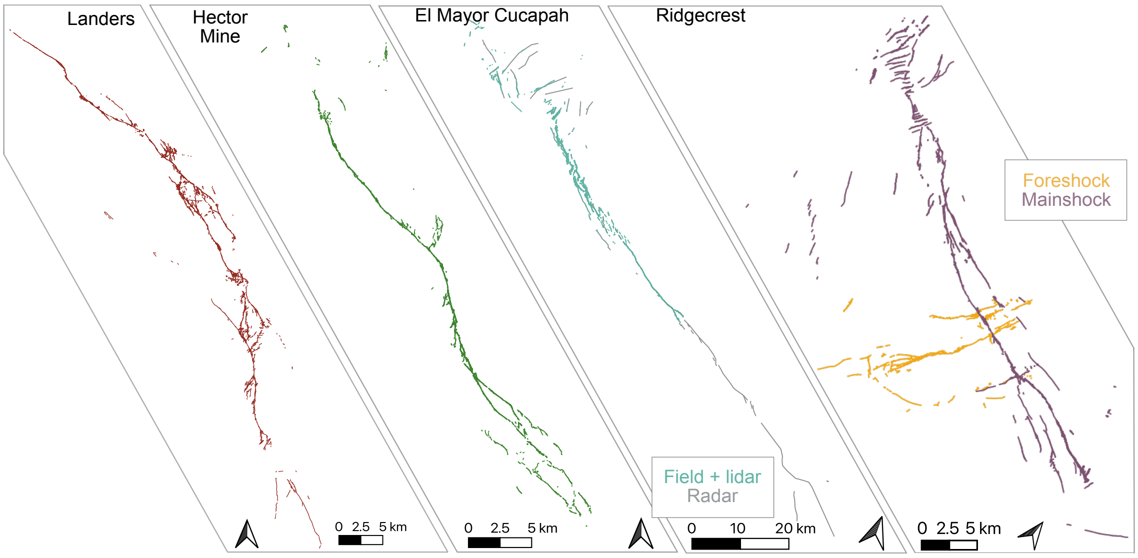

Figure 1: Surface rupture maps from the Landers, Hector Mine, El Mayor-Cucapah, and Ridgecrest earthquakes from the Fault Displacement Hazard Initiative database (Sarmiento et al., 2021). The gray lines in the El Mayor-Cucapah rupture are simplified traces mapped from radar data and excluded in this study. The turquoise lines were mapped from field and lidar data and included here. The purple lines in the Ridgecrest map represent mainshock rupture map and the orange lines represent the foreshock rupture map.

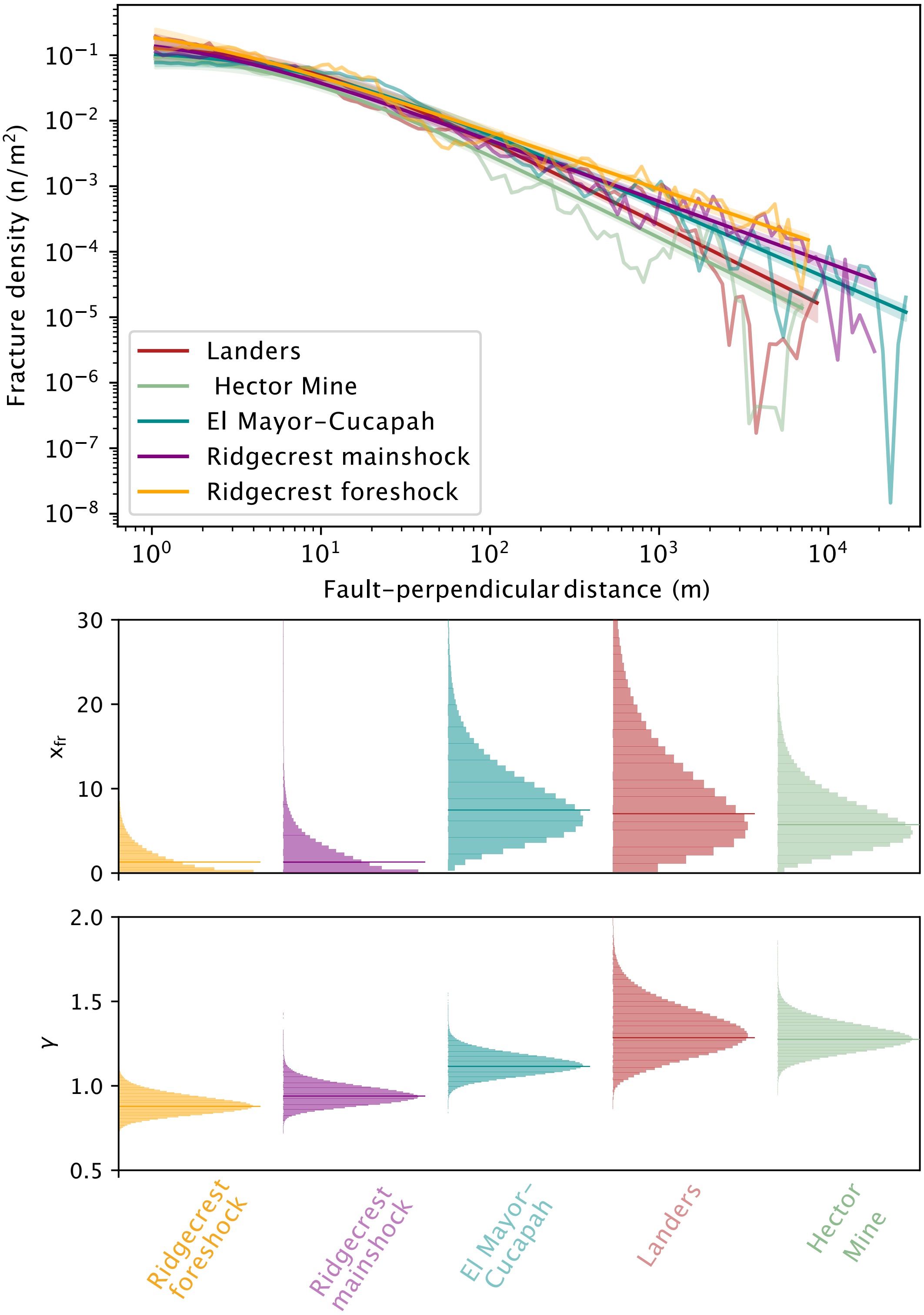

Figure 2: Rupture density distribution for the Landers, Hector Mine, El Mayor-Cucapah, and Ridgecrest earthquakes. The Ridgecrest foreshock and mainshock are shown as separate events. The shaded region represents the fits within one standard deviation of the maximum likelihood fit, shown as the bold line, fit using 2. The bottom panel shows the distribution of posterior values for γ, the scaling exponent of the density-distribution, and x_{fr}, the uncertainty on the location of the principal fault trace.

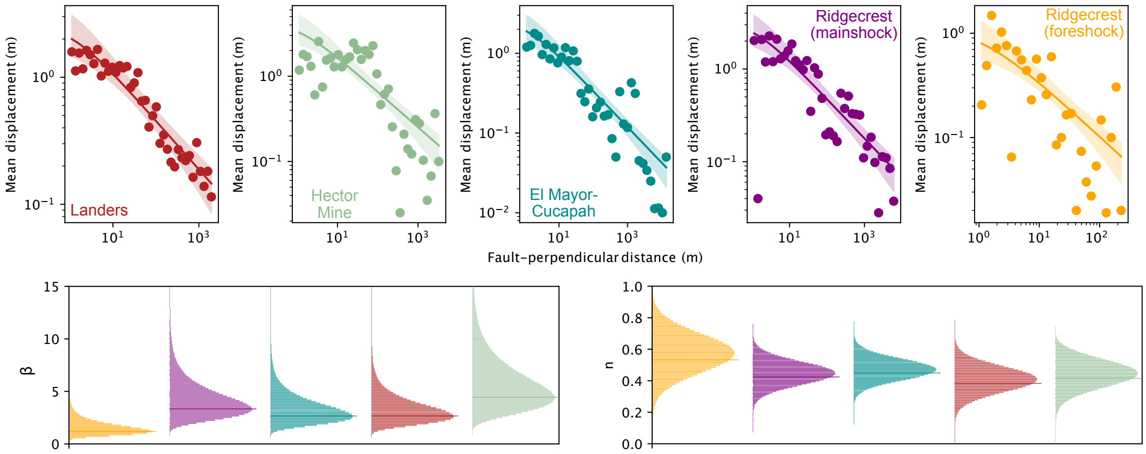

Figure 3: Distribution of average displacement measured in the field for the Landers, Hector Mine, El Mayor-Cucapah, and Ridgecrest earthquakes. The scattered dots on the top plot represent the field displacement data for each event from the FDHI database (Sarmiento et al., 2021). The solid lines represent the maximum likelihood fits to the distribution and the shaded area shows the 1σ posterior distribution from an MCMC fit. The bottom panels show the posterior distributions of β and n, fit using equation 3.

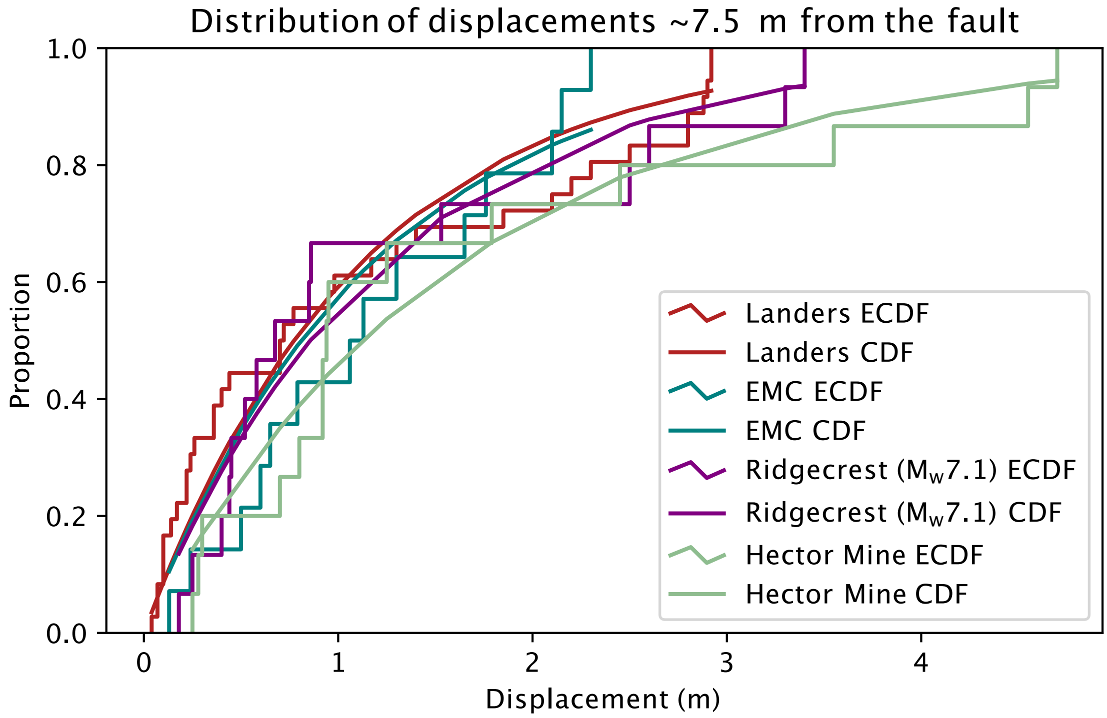

Figure 4: Empirical cumulative distribution function of the displacements 7.5 meters away from the fault for the Landers, Hector Mine, El Mayor-Cucapah, and Ridgecrest earthquakes. Note that we omit the Ridgecrest foreshock from this plot for clarity because the displacements are much smaller given the smaller magnitude. The cumulative distribution functions fit from the mean of the empirical data are plotted on top.

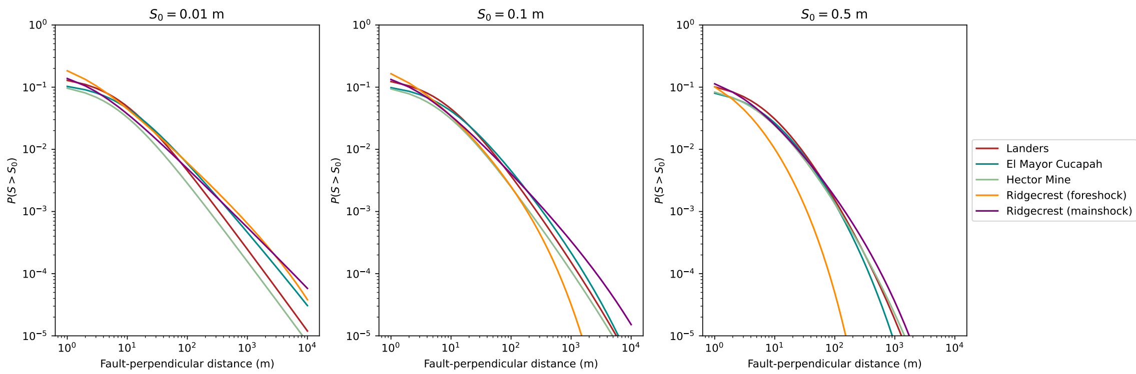

Figure 5: PFDHA model expressing the probability of finding a rupture hosting a displacement that exceeds threshold S_0 for the Landers, Hector Mine, El Mayor-Cucapah, and Ridgecrest earthquakes. The models are generated using equation 8. We show models for $S_0 = 0.01$ m, 0.1 m, and 0.5 m.

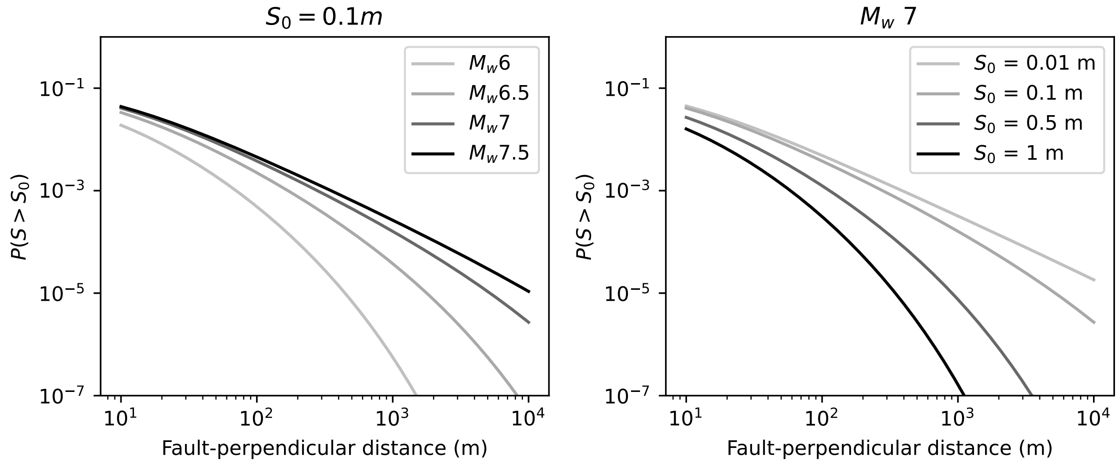

Figure 6: PFDHA model expressing the probability of finding a rupture hosting a displacement that exceeds threshold S_0 for a surface-rupturing strike-slip earthquake. The models are generated using equation 8. On the left, we show models for $M_w = 5$, 6, and 7, where $S_0 = 0.1$ m. On the right, we show models for $S_0 = 0.1$, 0.5, and 1 meter, for an M_w 7 event.

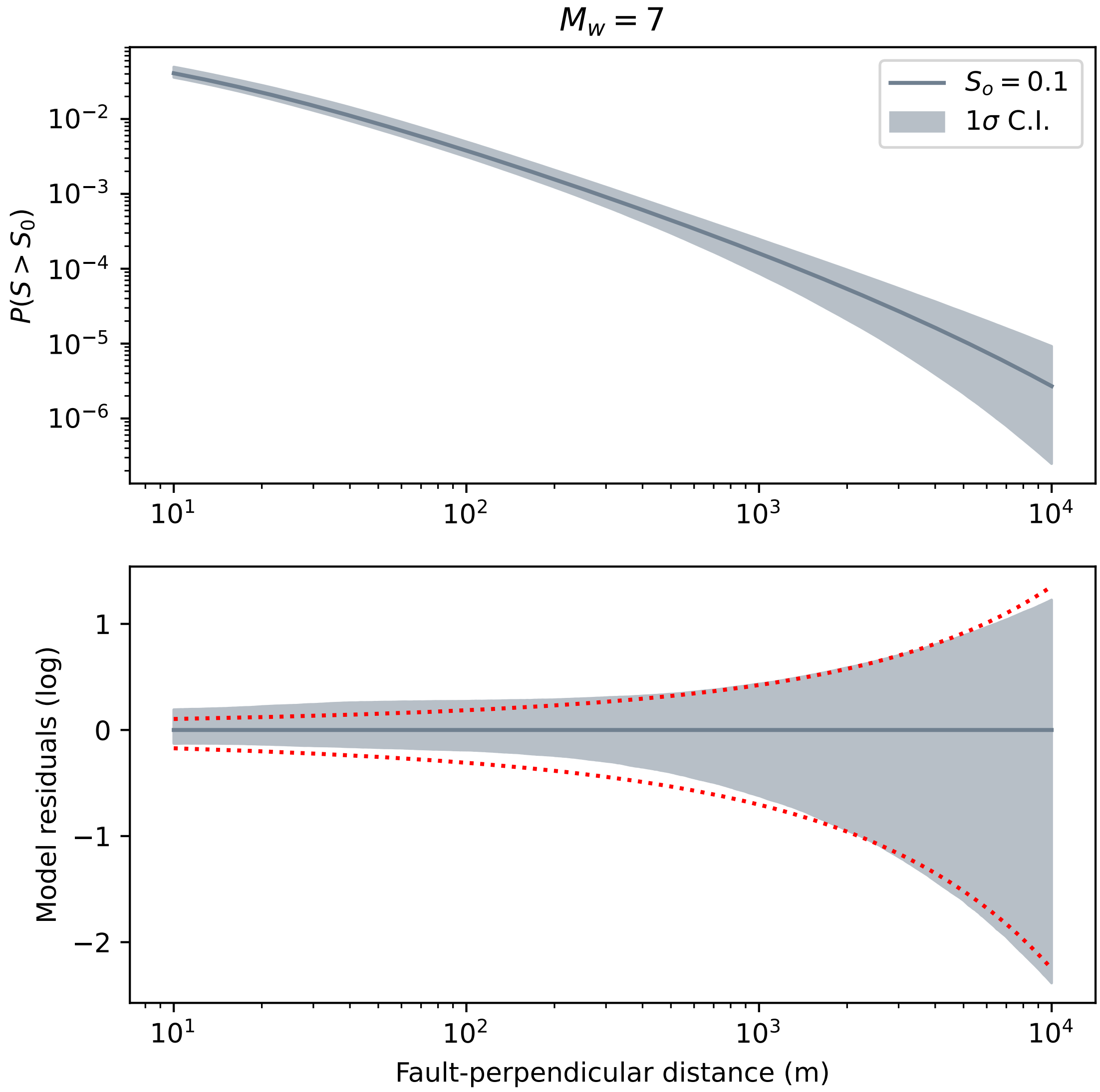

Figure 7: Top: PFDHA model expressing the probability of finding a rupture hosting a displacement that exceeds threshold $S_0 = 0.1$ m for a surface-rupturing strike-slip earthquake of M_w 7. The model is generated using equation 8. The shading represents the 1σ confidence intervals. The solid line represents the best-fit model. Bottom: Model residuals (log). The dotted red line represents the fit of equation 10 to the logarithmic of the residuals.

Parameter	Landers	Hector Mine	El Mayor-Cucapah	Ridgecrest (foreshock)	Ridgecrest (mainshock)	General model
v_0	0.15	0.28	0.12	0.31	0.20	0.13
x_{fr} (meters)	7.0	2.0	7.5	1.3	2.0	6.7
γ	1.3	1.2	1.1	0.9	0.9	1.2
β (meters)	2.7	4.4	2.7	1.2	3.3	$\beta(M_w)$
n	0.38	0.42	0.45	0.53	0.42	0.44

Table 1. Distribution of best-fit parameters for each event and the general model in equation 8.

Appendix

A Supplementary figures

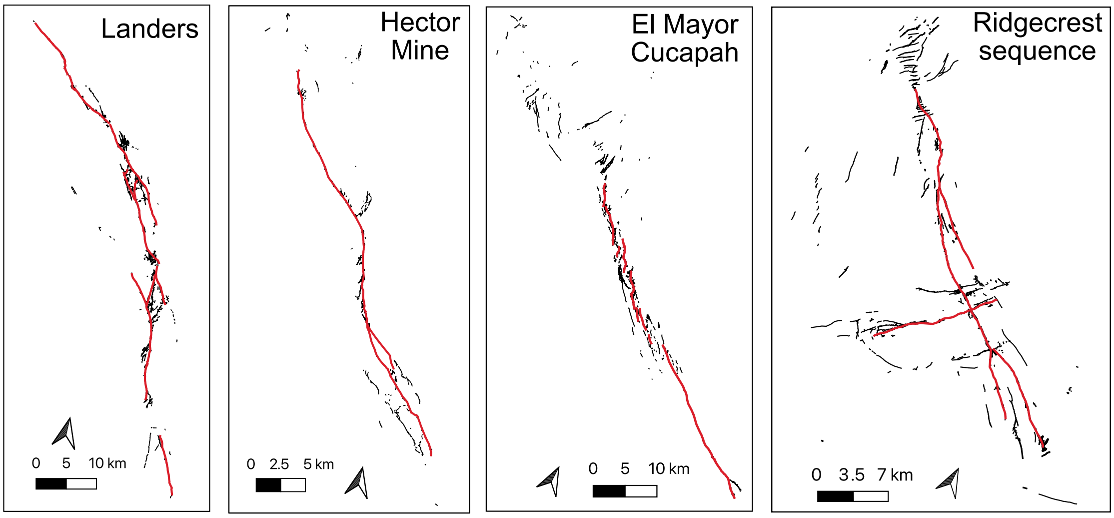

Figure A1: Secondary ruptures (black) and simplified principal rupture trace (red) for each event considered in this study.

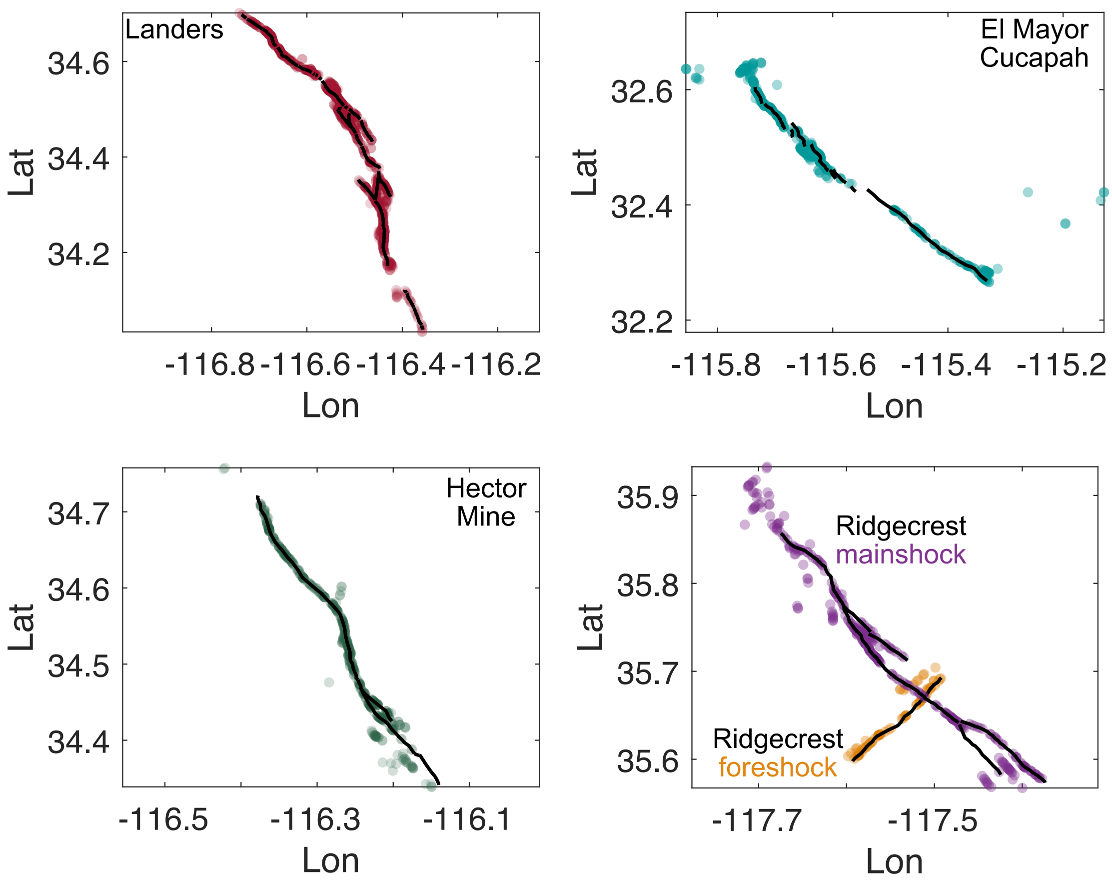

Figure A2: Displacement data from the Landers)(red), Hector Mine (green), El Mayor-Cucapah (teal), and Ridgecrest earthquakes (foreshock in orange and mainshock in purple) plotted over the principal rupture trace of each event. The displacement data is sourced from the Fault Displacement Hazard Initiative database (Sarmiento et al., 2021) and we only consider measurements collected in the field. The principal rupture traces are roughly simplified from the ruptures classified as primary in the FDHI database (see figure A1) in the appendix.

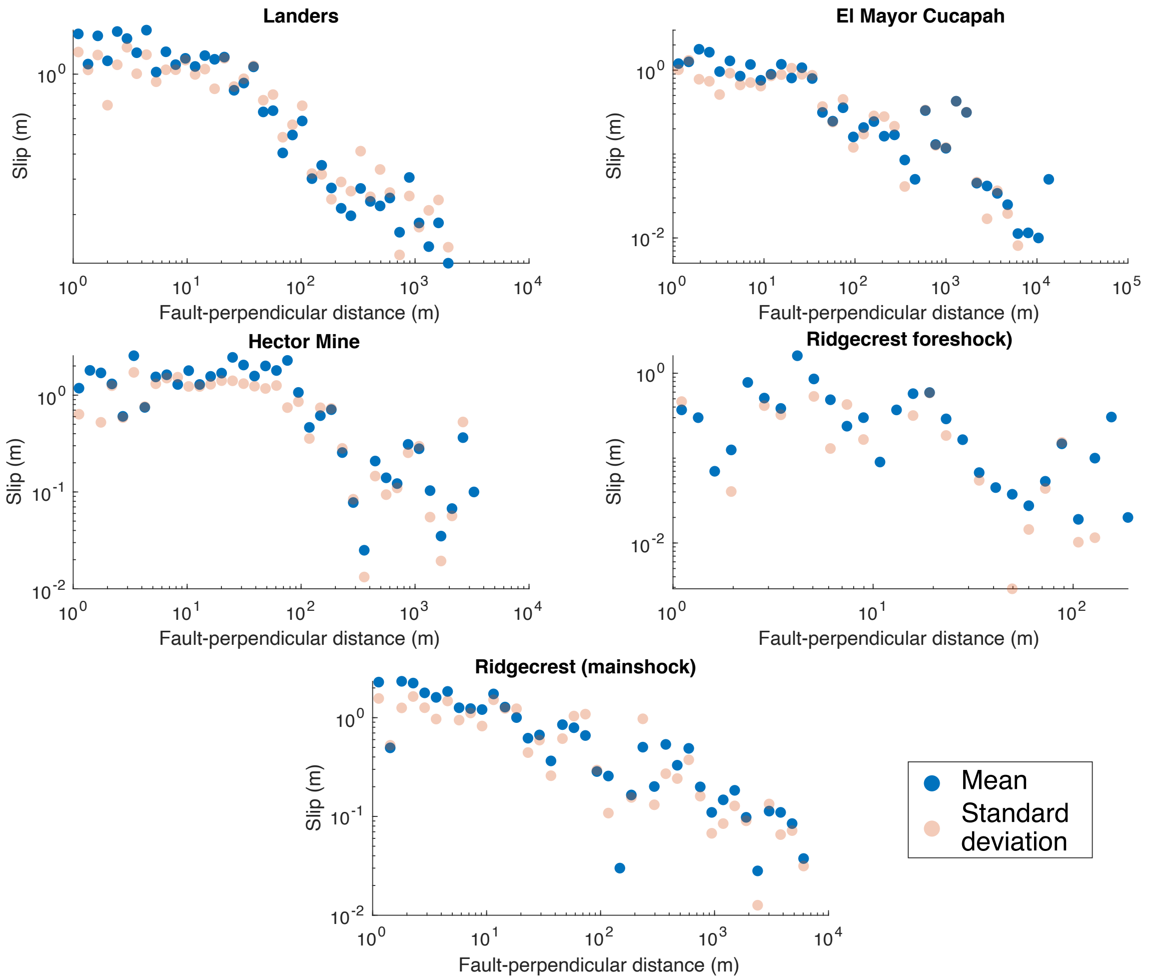

Figure A3: Mean (blue) and standard deviation (pink) of slip with fault-perpendicular distance for the Landers, Hector Mine, El Mayor-Cucapah, and Ridgecrest earthquakes. The consistent correlation of the mean and the standard deviation suggests the displacements are exponentially distributed within each distance bin.

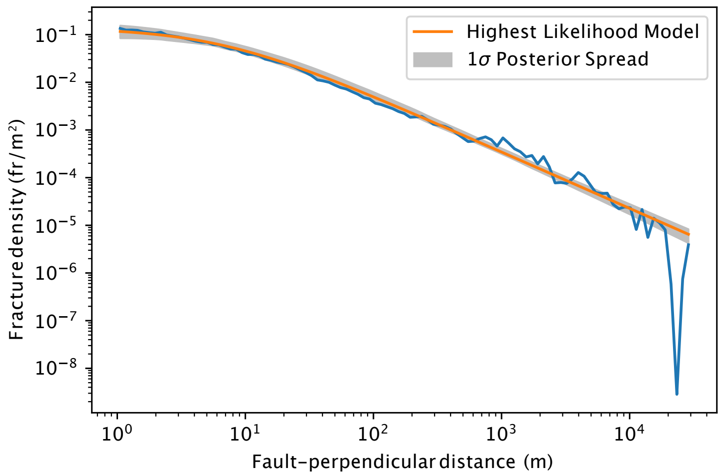

Figure A4: General model for the decay of rupture density with fault-perpendicular distance generated from combining the secondary rupture maps from the Landers, Hector Mine, El Mayor-Cucapah, and Ridgecrest earthquakes.

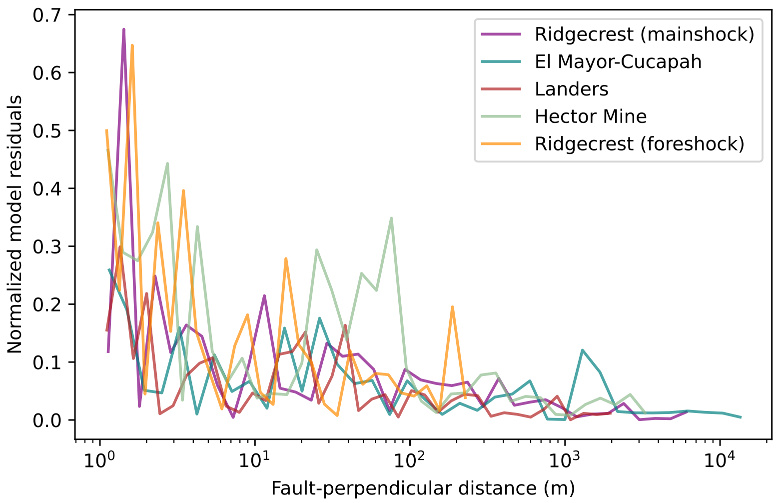

Figure A5: Model residuals from the fits of equation 3 to the field displacement data in the FDHI database for each event (figure 3). The residuals are normalized by the value of β for each event to account for the magnitude-dependence of displacement.

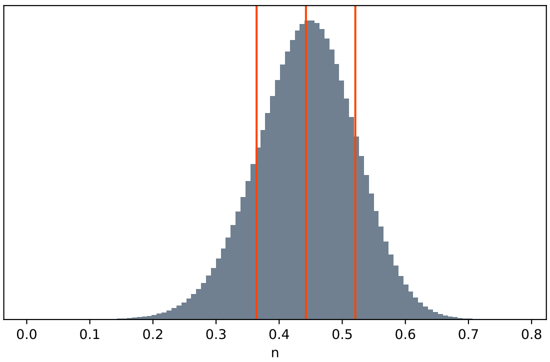

Figure A6: Concatenated posteriors for n in equations 3 and 8 from the Landers, Ridgecrest mainshock, and El Mayor-Cucapah event. Note that n is roughly normally distributed. The vertical red lines indicate the mean and data within one standard deviation of the mean.

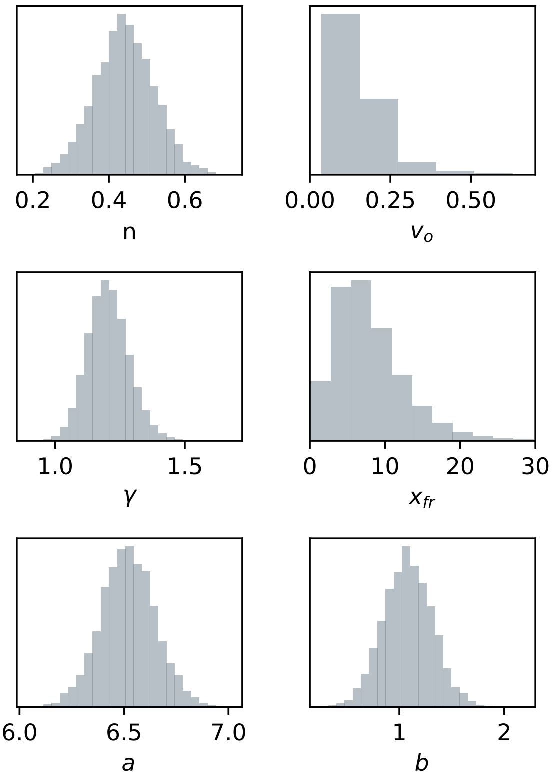

Figure A7: Distribution of parameters from equation 8. ν_o, x_{fr}, and γ are sampled from the posterior distributions of the fits in supplementary figure A4. n, a, and b are sampled from normal distributions where the mean and standard deviation are calculated in this study for n (figure A6 in the appendix) and in Brengman et al. (2019) for a and b.

Supplementary methods

We build on the method in Rodriguez Padilla et al. (2022b) to estimate the decay of rupture density with fault-perpendicular distance for each event. We begin by discretizing every rupture into 1m spaced points, to minimize the effect of mapper bias in rupture continuity. Next, we measure the distance between each point and the nearest point on the main rupture. The principal rupture is simplified for each event from the cracks defined as primary in the FDHI rupture database (supplementary figure A1). We then log bin the distances into 100 bins, from 0 to the furthest rupture from the main rupture, and count the number of rupture segments per bin. Last, we normalize each bin by its size, and the entire decay by the total length of the principal fault. This produces the decays shown in Figure 2.

We fit each decay with an affine-invariant ensemble sampler for Markov Chain Monte Carlo (Goodman and Weare, 2010; Foreman-Mackay et al., 2013) to estimate the maximum likelihood parameters for equation 2. As priors, we use uniformly distributed values of ν_o= (0,3), x_{fr}= (0, 100) meters, and γ = (0, 3). We assume that the error of $\nu(x)$ in each bin is Poisson-distributed, following the method of Powers and Jordan (2010). We employ an ensemble of 200 walkers, which run for 100,000 iterations, following a 10,000-iteration burn-in period.

We follow a similar approach to estimate the decay of average displacement with fault-perpendicular distance. We take the displacements from the FDHI database for each event and measure their distance to the principal rupture trace (supplementary figure A1. We then log-bin the distances into 40 bins, from 0 to the furthest rupture from the main rupture, and calculate the average displacement per bin. This produces the decays shown in Figure 3. We fit each decay with an affine-invariant ensemble sampler for Markov Chain Monte Carlo (Goodman and Weare, 2010; Foreman-Mackay et al., 2013) to estimate the maximum likelihood parameters for equation 3. As priors, we use uniformly distributed values of β= (0,15) meters and n=(0,3). We employ an ensemble of 200 walkers, which run for 100,000 iterations, following a 10,000-iteration burn-in period. Note that we fix $x_S = 1$ meter in equation 3 because this provides a better model fit than letting x_S be a free parameter that is fit with the ensemble sampler for MCMC and contributes to reducing uncertainty in the model fits. We also tested values of $x_S = 10$ meters, with worse residuals, thus the choice of $x_S = 1$ meter.

Supplemental references

1. Foreman-Mackey, D., Hogg, D. W., Lang, D., & Goodman, J. (2013). emcee: the MCMC hammer. Publications of the Astronomical Society of the Pacific, 125(925), 306.

2. Goodman, J., & Weare, J. (2010). Ensemble samplers with affine invariance. Communications in applied mathematics and computational science, 5(1), 65-80.

3. Powers, P. M., & Jordan, T. H. (2010). Distribution of seismicity across strike-slip faults in California. Journal of Geophysical Research: Solid Earth, 115(B5).